

Laser-driven droplet deformation at low Weber numbers

Mikheil Kharbedia¹, Hugo França^{1,2}, Hermann Karl Schubert,¹
Dion Engels¹ , Maziyar Jalaal²  and Oscar Versolato^{1,3} 

¹Advanced Research Center for Nanolithography (ARCNL), Science Park 106, 1098 XG Amsterdam, The Netherlands

²Van der Waals-Zeeman Institute, Institute of Physics, University of Amsterdam, Science Park 904, Amsterdam 1098XH, The Netherlands

³Department of Physics and Astronomy and LaserLaB, Vrije Universiteit Amsterdam, De Boelelaan 1100, 1081 HV, Amsterdam, The Netherlands

Corresponding author: Oscar Versolato, versolato@arcnl.nl

(Received 29 August 2025; revised 9 January 2026; accepted 17 March 2026)

We investigate droplet deformation following laser-pulse impact at low Weber numbers ($We \sim 0.1-100$). Droplet dynamics can be characterised by two key parameters: the impact Weber number and the width, W , of the distribution of the impact force over the droplet surface. By varying laser-pulse energy, our experiments traverse a phase space comprising (i) droplet oscillation, (ii) breakup or (iii) sheet formation. Numerical simulations complement the experiments by determining the pressure width and by allowing We and W to be varied independently, despite their correlation in the experiments. A single phase diagram, integrating observations from both experiments and simulations, demonstrates that all phenomena can be explained by a single parameter: the deformation Weber number $We_d = f(We, W)$ that is based on the initial radial expansion speed of the droplet, following impact. The resulting phase diagram separates (i) droplet oscillation for $We_d < 5$, from (ii) breakup for $5 < We_d < 60$ and (iii) sheet formation for $We_d > 60$.

Key words: drops, drops and bubbles

1. Introduction

Upon impacting a solid surface, the momentum of a falling droplet is counterbalanced by inertia, viscous dissipation and surface tension, which governs fluid retraction (Pasandideh-Fard *et al.* 1996; Josserand & Thoroddsen 2016). The resulting deformation

exhibits complex dynamics, including oscillations, sheet formation during spreading and jetting upon retraction (Yarin & Weiss 1995; Zhang *et al.* 2022). Similarly rich dynamics is observed when droplets splash on pillars (Villermaux & Bossa 2011; Wang *et al.* 2018). Deformations may also occur under the influence of external flows where a wide range of phenomena from droplet vibration (Pilch & Erdman 1987; Hsiang & Faeth 1992) to bag breakup (Guildenbecher, López-Rivera & Sojka 2009; Jalaal & Mehravaran 2012; Jackiw & Ashgriz 2021), sheet stripping (Theofanous 2011; Jalaal & Mehravaran 2014) and catastrophic fragmentation (Guildenbecher *et al.* 2009; Theofanous 2011) may occur. The resulting dynamics is often characterised by the Weber number, $We = \rho D_0 U^2 / \sigma$ (with the liquid density ρ in droplet impact experiments, droplet diameter D_0 , impact velocity U and surface tension σ ; for wind-driven droplet fragmentation, the relevant air density and velocity are taken instead), and the Ohnesorge number that relates the viscous forces to inertial and surface tension forces. In contrast to previous methods, using a laser impact on a droplet offers a unique opportunity to precisely control the pressure profile on its surface. In wind tunnel experiments, the entire surrounding medium is in motion, which complicates any effort to stabilise or adjust the pressure profile on the droplet surface. Similarly, when employing a fixed pillar to perturb the droplet, the pillar remains in continuous contact with the droplet, and neither the tunnel nor the pillar technique provides instantaneous control. As a result, in all these approaches, the droplet's response is primarily determined by the impact velocity U .

Nevertheless, the force distribution on the surface is well known to significantly influence droplet deformation behaviour at high We (Gelderblom *et al.* 2016; Hernandez-Rueda *et al.* 2022; França *et al.* 2025), as established in the context of laser-driven droplet deformation for nanolithography (Versolato 2019). The interaction between nanosecond-pulsed laser light with micrometre-sized tin droplets is a relevant source of extreme ultraviolet (EUV) light, as used in state-of-the-art industrial nanolithography. The generation of EUV light involves the laser-impact deformation of a tin droplet into a thin sheet that is subsequently laser-heated into an EUV-emitting plasma. Upon (~ 10 mJ) laser-pulse impact, a plasma is generated from the droplet surface and produces a recoil pressure of the order of ~ 100 kbar. In a typical setting, the droplet is accelerated on the laser-pulse length scale, $\tau_p \sim 10$ ns, reaching terminal velocities of the order of $U \sim 100$ m s $^{-1}$ while it radially expands. The corresponding large Weber number is in the range ~ 1000 – $10\,000$; hence, the droplet transforms into a time-varying radially expanding liquid sheet (Kurilovich *et al.* 2016, 2018; Liu *et al.* 2021, 2023), undergoing several hydrodynamical instabilities responsible for its rupture through hole opening (Klein *et al.* 2020a) or radial accumulation of the liquid into a fragmenting bounding rim (Wang *et al.* 2018; Wang & Bourouiba 2021).

Laser-induced droplet deformation has been shown to be well described by the impact propulsion Weber number $We = \rho D_0 U^2 / \sigma$, based on centre-of-mass propulsion velocity U , and deformation Weber number (Klein *et al.* 2020b; Liu *et al.* 2022) $We_d = \rho D_0 \dot{R}_0^2 / \sigma$, based on radial expansion rate \dot{R}_0 ; these two orthogonal velocities, as shown in figure 1, are correlated and both increase with increasing laser-pulse energy (Gelderblom *et al.* 2016; Hernandez-Rueda *et al.* 2022). Additionally, to properly account for the droplet curvature after laser impact, França *et al.* (2025) described the resulting pressure profile in terms of a raised cosine function projected on the surface $\sim (1 + \cos(\theta\pi/W))H(W - \theta)$ (figure 1a,b), where W is a dimensionless pressure width and $H(W - \theta)$ is the Heaviside step function. This parameter W can be interpreted as a measure of the spatial, angular extent of the pressure imprinted on the droplet by the laser plasma, as illustrated in figure 1(a): increasing W leads to a broader pressure field on the droplet, which manifests

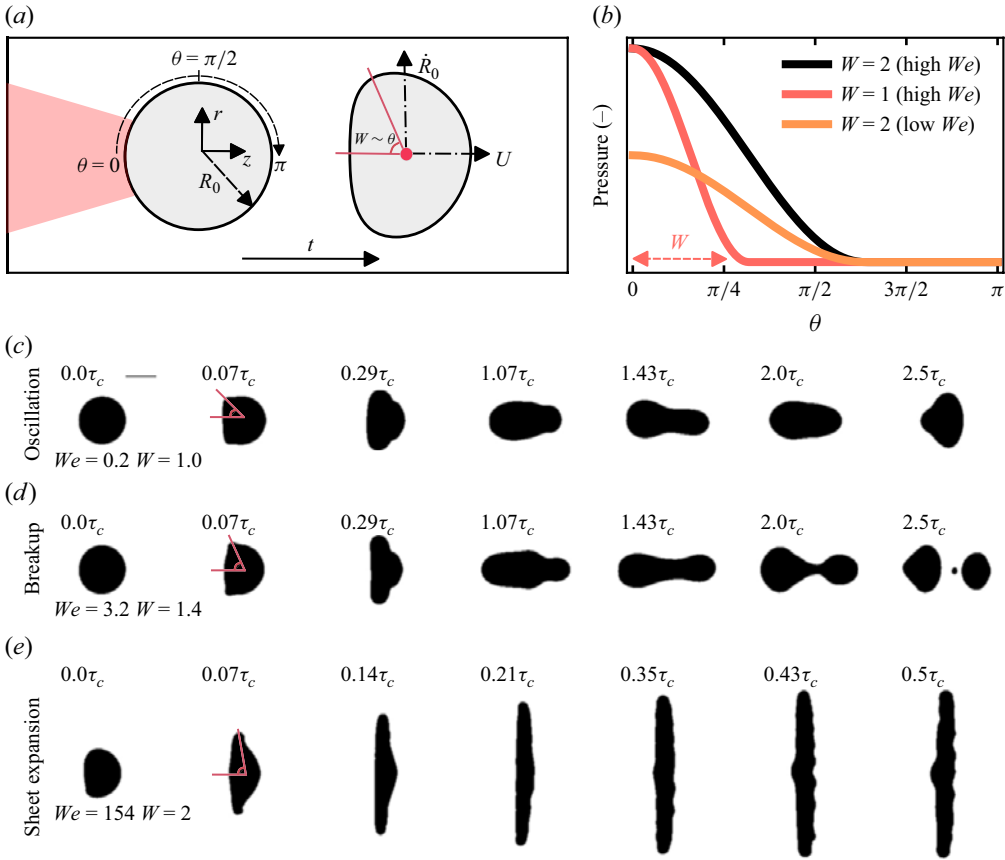


Figure 1. (a) Conceptual side-view representation of laser–droplet interaction. The laser beam is represented as a red area. After laser impact, the droplet is propelled axially at U while radially expanding at \dot{R}_0 initially. The force profile resulting from laser–plasma interaction, described as a dimensionless parameter W , is proportional to early-time deformation (see main text). The angular distribution of the resulting pressure is depicted in (b) where curves show different values of pressure distribution on the droplet’s surface. The black and orange curves with the same value of W depict different values of We (higher and lower, respectively). The dashed line illustrates the width of the pressure distribution for $W = 1$. (c–e) Experimental examples of the hydrodynamic response after laser interaction with a droplet with diameter $D_0 = 50 \mu\text{m}$. Each row contains frames at different fractions of capillary times, $\tau_c = 16.4 \mu\text{s}$. (c) Droplet oscillation for $We = 0.2$ and $W = 1.0$. (d) Droplet breakup after retraction for $We = 3.4$ and $W = 1.4$. (e) Sheet expansion for $We = 154$ and $W = 2$. The grey scale bar in the first frame in (c) corresponds to $D_0 = 50 \mu\text{m}$.

as a broader early-time deformation characterised by a larger opening angle θ_{open} (figure 1a,c–e). Further details are discussed in § 3.1. This pressure profile accurately describes the sheet morphology over a range of pressure widths $1 < W < 2.5$ as shown by França *et al.* (2025). We illustrate the impact of the propulsion We with the pressure width W on the pressure field separately in figure 1(b) (see § 2.2). The three parameters (We , We_d , W) are correlated and the function $We_d = f(We, W)$ is set by an initial, instantaneous pressure profile with essentially two free parameters being its amplitude and width (França *et al.* 2025) (see § 3.1). For a more comprehensive study of the separate influence of laser spot size, droplet diameter and laser-pulse energy on the plasma-induced velocities (U , \dot{R}_0) we refer the reader to Hernandez-Rueda *et al.* (2022).

Thus, unlike droplet impact on solid surfaces, falling drop or wind tunnel interactions, laser–droplet interaction offers a path to studying how the spatial distribution of the force, along with its overall magnitude, influences droplet dynamics. However, motivated by direct nanolithography applications, prior studies have focused on high Weber numbers that lead to sheet formation.

In this work, we investigate droplet deformation following laser-pulse impact at low Weber numbers ($We \sim 0.1–100$) combining experiments with numerical simulations. Decreasing markedly the pulse energy ($\sim 0.1–1$ mJ) in the experiment, we mainly focus on the dynamics of the regimes before sheet formation. In [figure 1\(c–e\)](#) we illustrate representative cases of droplet deformation over fractions of the capillary time $\tau_c = \sqrt{\rho D_0^3/6\sigma}$, with ρ and σ being liquid density and surface tension, respectively. At lower We , an oscillatory motion is observed, as shown in [figure 1\(c\)](#), reminiscent of previous work on oscillating free droplets (see e.g. Becker, Hiller & Kowalewski 1991; Hsiang & Faeth 1992; Bostwick & Steen 2009; Rimbert *et al.* 2020; Parik, Truscott & Dutta 2024). The symmetry of this oscillation is unavoidably broken given the laser impact geometry. For slightly higher pulse energies the droplet breaks up, as shown in [figure 1\(d\)](#). Finally, at even higher pulse energies, the radial inertia leads to sheet formation, as shown in [figure 1\(e\)](#). For reference, we provide estimates of the corresponding (We , W) values for each case in [figure 1](#), with W obtained using a scaling relation that also involves input from our simulations (see below). The two parameters are strongly correlated in the experiment, with increased pulse energy leading to both increased We and W values. The goal of this study is to characterise the individual influence of these two key parameters on the deformation process for low We . Our experiments traverse a phase space comprising (i) droplet oscillation, (ii) breakup and (iii) sheet formation. Numerical simulations complement the experiments and allow for independently varying We and W .

The rest of this article is organised as follows. In § 2.1 we provide a brief explanation of our experimental set-up. § 3 is devoted to the presentation and discussion of the results. The numerical simulations are explained in § 2.2. Next, in § 3.1 we perform an analysis of the pressure profile on the droplet, where we explain how to correlate the droplet inertial deformation with the corresponding pressure projection on the surface. The oscillatory motion of the droplet is discussed in § 3.2. In § 3.3, we illustrate the breakup mechanism and how a further increase in the energy of the laser pulse leads to the familiar scenario where the tin droplet deforms into a radially expanding sheet. To summarise, in § 3.5 we present a phase diagram, combining experiments and simulations, based on the systematic variation of both We and pressure width W and discuss the boundaries for the different phases.

2. Methods

2.1. Experimental method

We refer the reader to Kurilovich *et al.* (2018) and Meijer *et al.* (2022b) for a detailed description of the experimental set-up. Briefly, we use a micro-sized tin liquid jet produced from a pressurised tank placed on the top of a spherical vacuum chamber kept at a base pressure of 10^{-6} mbar. The jet is fragmented into a train of equally spaced droplets, depending on the frequency of the voltage pulses applied to the nozzle (Kurilovich *et al.* 2018). In the current experiments, we produce two different droplet sizes, with diameters $D_0 = 50, 70 \mu\text{m}$, with density $\rho = 7000 \text{ kg m}^{-3}$, surface tension $\sigma = 0.544 \text{ N m}^{-1}$ and dynamic viscosity $\mu = 1.8 \times 10^{-3} \text{ Pa s}$. The droplet interacts with a circularly polarised 1064 nm Nd:YAG laser pulse, with a Gaussian temporal profile of 6 ns and peak energies

| D_0 (μm) | τ_c (μs) | E_p (mJ) | U (m s^{-1}) | \dot{R}_0 (m s^{-1}) | Re | We |
|-------------------------|----------------------------|------------|---------------------------|-----------------------------------|---------|----------|
| 50 | 16.4 | 0.3–6 | 0.17–15 | 0.02–24 | 33–3100 | 0.02–160 |
| 70 | 27.1 | 0.2–4 | 0.20–8.7 | 0.05–10 | 54–2400 | 0.04–68 |

Table 1. Representative parameters of this study include droplet diameter, D_0 , capillary time, τ_c , laser-pulse energy, E_p , propulsion velocity, U , radial expansion rate, \dot{R}_0 , and dimensionless numbers like propulsion Reynolds number, Re , and propulsion Weber number, We . Note that the values are indicated as approximate ranges considered in this study.

in the range $E_p = 0.3\text{--}5$ mJ. The laser is focused on the droplet as a Gaussian spot with a diameter of $\sim 85 \mu\text{m}$ at full width at half-maximum (FWHM); the focus is not changed throughout the experiments. To visualise the laser–droplet interaction, we use a stroboscopic imaging system, based on illuminating the droplet with a temporally and spatially incoherent green light, with a wavelength of 564 ± 10 nm and temporal resolution of 5 ns. Droplets are illuminated in the centre of the chamber with this light at two different angles, 90° and 30° , with respect to the laser propagation axis, imaging the droplet from side view and nearly front view, respectively. The corresponding shadow image is collected with a CCD camera. The axial propulsion and radial expansion rates of the droplet are determined within the first three delays ~ 600 ns after laser impact. Typical values of the velocities explored in this study are listed in table 1. In order to precisely synchronise the onset of laser-pulse impact and shadowgraph recording with the cameras, the laser system is triggered by a delay generator. The frame acquisition rate is set to be equal to the laser repetition rate at 10 Hz. Given the reproducibility of our experiments, we can trace the time evolution of the droplet after laser impact with a precision of a few nanoseconds. This is performed by delaying the illumination pulse after the laser pulse. In the following, we scan the illumination pulse with time steps of 200 ns, over several capillary times.

2.2. Computational method

We perform simulations to numerically predict the laser-induced deformation of a tin droplet at low Weber numbers. Assuming good alignment between the laser and the droplet, the resulting axisymmetry allows the droplet dynamics (which in this work does not include the parameter space relevant for late-time radial, axisymmetry-breaking ligaments and ligament fragments (Wang *et al.* 2018)) to be captured using two-dimensional (in cylindrical coordinates) simulations (Gelderblom *et al.* 2016; França *et al.* 2025). The governing equations for the isothermal incompressible bi-phase (droplet and ambient) flow are the continuity and momentum conservation, given by

$$\rho \left(\frac{\partial \mathbf{u}}{\partial t} + \nabla \cdot (\mathbf{u}\mathbf{u}) \right) = -\nabla p + \nabla \cdot (2\mu \mathbf{D}) + \mathbf{f}_\sigma, \quad (2.1)$$

$$\nabla \cdot \mathbf{u} = 0, \quad (2.2)$$

where \mathbf{u} and p are the velocity and pressure fields, $\mathbf{D} = [\nabla \mathbf{u} + (\nabla \mathbf{u})^T]/2$ is the deformation rate tensor and ρ and μ are the fluid density and viscosity, respectively. We note that, in this one-fluid formulation, ρ and μ are functions with values that change across the droplet–ambient interface. The expression for these functions is given later in this paragraph. In the numerical method used here, the surface tension force is defined as a body force $\mathbf{f}_\sigma = \sigma \kappa \delta_s \mathbf{n}$, where κ is the local curvature of the interface, σ is the constant surface tension coefficient, \mathbf{n} is the unit vector normal to the interface and δ_s is the Dirac delta function centred on the interface (Popinet 2009; Tryggvason, Scardovelli &

Zaleski 2011). The droplet interface is tracked using a volume-of-fluid scheme (Hirt & Nichols 1981), in which a scalar colour function $c(\mathbf{x}, t)$ indicates the fraction of droplet fluid contained in each numerical cell. The local density and viscosity are obtained by linearly interpolating using the value of c . So ρ and μ from (2.1) are defined as

$$\rho(c) = c \rho_d + (1 - c)\rho_a, \tag{2.3}$$

$$\mu(c) = c \mu_d + (1 - c)\mu_a, \tag{2.4}$$

where the indices d and a refer to the properties of the droplet and ambient fluids, respectively. While in experiments the droplet is contained within a vacuum chamber, due to numerical limitations, we keep the ambient fluid properties set to $\rho_a = 10^{-3}\rho_d$ and $\mu_a = 10^{-3}\mu_d$.

Equations (2.1)–(2.2) can be non-dimensionalised by rescaling variables with the following choices:

$$\mathbf{x} = D_0 \bar{\mathbf{x}}, \quad t = \frac{D_0}{U} \bar{t}, \quad \mathbf{u} = U \bar{\mathbf{u}}, \quad p = \rho U^2 \bar{p}, \quad \kappa = \frac{1}{D_0} \bar{\kappa}, \quad \delta_s = \frac{1}{D_0} \bar{\delta}_s, \tag{2.5}$$

where D_0 is the diameter of the droplet and U is the droplet propulsion velocity obtained after the laser interaction.

Substituting (2.5) into (2.1)–(2.2), we obtain the non-dimensional version of the governing equations, given by

$$\bar{\rho} \left(\frac{\partial \bar{\mathbf{u}}}{\partial \bar{t}} + \nabla \cdot (\bar{\mathbf{u}} \bar{\mathbf{u}}) \right) = -\nabla \bar{p} + \frac{1}{Re} \nabla \cdot (2\bar{\mu} \bar{\mathbf{D}}) + \frac{1}{We} \bar{\kappa} \bar{\delta}_s \mathbf{n}, \tag{2.6}$$

$$\nabla \cdot \bar{\mathbf{u}} = 0, \tag{2.7}$$

where

$$Re = \frac{\rho_d U_z D_0}{\mu_d} \quad \text{and} \quad We = \frac{\rho_d U_z^2 D_0}{\sigma} \tag{2.8}$$

are the Reynolds and Weber numbers, respectively. The non-dimensional density and viscosity functions are obtained from (2.3)–(2.4) and are given by

$$\bar{\rho}(c) = c + (1 - c)\rho_a/\rho_d, \tag{2.9}$$

$$\bar{\mu}(c) = c + (1 - c)\mu_a/\mu_d. \tag{2.10}$$

Equations (2.6)–(2.7) are numerically solved using the open-source free software language Basilisk C (Popinet & Collaborators 2013–2021). The droplet is created at the centre of a square domain $[-5D_0, 5D_0] \times [-5D_0, 5D_0]$ that is fully discretised with a non-uniform quadtree grid (Popinet 2003, 2009). To accurately resolve the flow structure inside the droplet and its shape, we apply increased refinement levels for the liquid phase and also at the interface. The maximum quadtree level of refinement used is 13, resulting in grid cells with a minimum size of $\Delta = 10D_0/(2^{13}) = 0.0012D_0$.

The volume fraction field c is then advected over time by solving the equation

$$\frac{\partial c}{\partial t} + \nabla \cdot (c \mathbf{u}) = 0. \tag{2.11}$$

The numerical code then solves the governing equations using a projection method and a multilevel Poisson solver. More details of the volume-of-fluid implementation, including extensive numerical validation of the software language Basilisk C, can be found in many other works involving deformable surfaces Popinet (2009, 2015), and more recent test cases such as Sanjay, Lohse & Jalaal (2021), Gai *et al.* (2025), Guan *et al.* (2025), Harris *et al.* (2026), Mou *et al.* (2026), Patel & Zhou (2026).

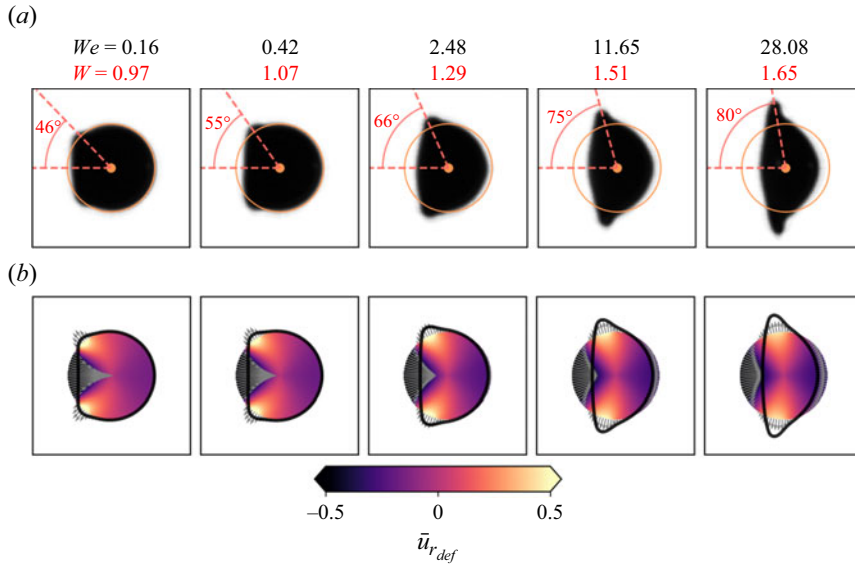


Figure 2. Droplet early deformation for different pressure profiles imprinted by the laser pulse. (a) Quantification of initial droplet deformation on laser-faced side within the inertial time scale, at $200 \text{ ns} \sim 0.01 \tau_c$. The impulsed liquid flow manifests as two bulges that display certain opening angles. The orange circle represents the shape of the droplet before laser impact. (b) Corresponding simulations with the same We values with a W parameter selected to match the angle of the surface maximum radial velocity with the corner bulges shown in (a). The grey arrows define the velocity field of the liquid upon laser impact, whereas the colourmap shows the radial component of the velocity, $\bar{u}_{r,def}$. The black contour represents the droplet morphology at $0.01 \tau_c$.

The interaction between laser pulse and droplet is modelled through the approach of Gelderblom *et al.* (2016) as also detailed in França *et al.* (2025). This approach relies on the assumption that the pressure impulse experienced by the droplet occurs on a time scale much smaller than any of the relevant hydrodynamic scales. Within this very short time span, we assume that the flow inside the drop is inviscid, irrotational and incompressible, resulting in the classical Laplace equation ($\nabla \bar{p} = 0$) for potential flows. This equation is solved semi-analytically in spherical coordinates within the droplet by imposing the chosen pressure profile (see figure 1a,b) as a boundary condition on the drop surface. From the obtained pressure field, the potential flow assumption gives a velocity field that can be calculated through $\bar{\mathbf{u}}_0 = -\nabla \bar{p}$. This velocity field is used as an initial condition for the full Navier–Stokes equations (2.6)–(2.7), which are then solved in time and space according to the scheme described above. For validation of the numerical methods employed, we refer the reader to França *et al.* (2025) and in particular the detailed appendices therein.

3. Results and discussion

3.1. Droplet deformation and pressure profile

Our study requires knowledge of both propulsion We and the width W of the pressure profile. The latter is related to plasma pressure and cannot be directly obtained from experimental shadowgraphy images that track the liquid mass. However, the fingerprint of the pressure profile appears as an early surface deformation on the side facing the laser, measurable at the first available frame at $200 \text{ ns} \sim 0.01 \tau_c$. In figure 2(a), for $We = 0.16$, we can see a small bulge with a certain opening angle $\theta_{open} \sim 46^\circ$. This value increases

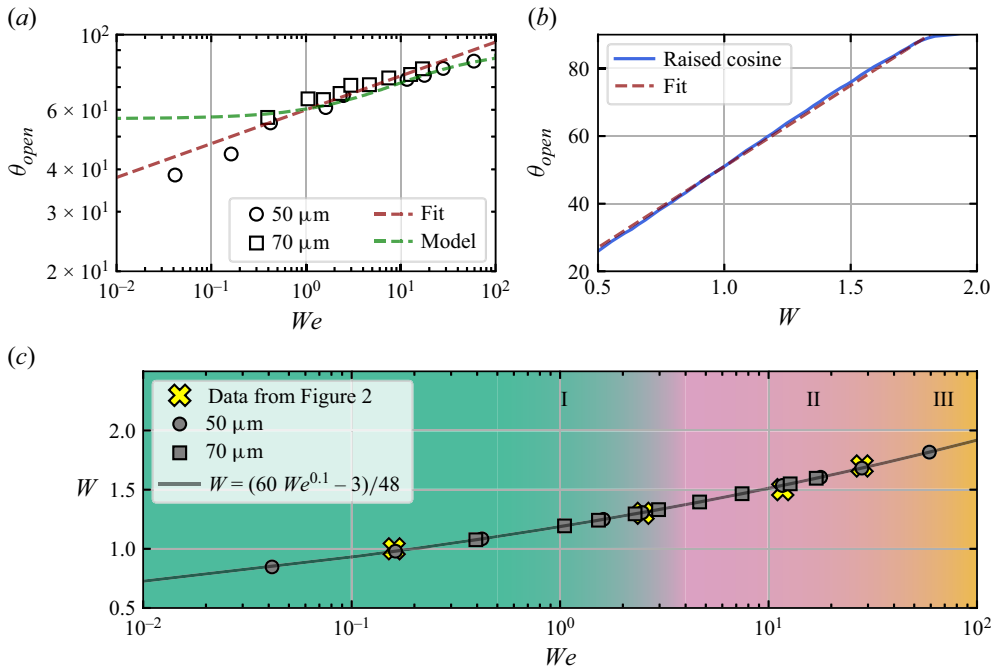


Figure 3. Correlation between the propulsion We and the pressure width W . (a) Opening angle θ_{open} against We for two droplet diameters, $D_0 = 50, 70 \mu\text{m}$. The red dashed line represents the empirical fit to the experimental data, with $\theta_{open} = 60We^{0.1}$. The green dashed line depicts the numerical result from the model. See main text. (b) Variation of θ_{open} for different pressure widths W as observed from simulations. The red dashed line depicts the numerical scaling found from simulations, with $\theta_{open} = 48W + 3$. (c) Variation of W with We . The grey circles correspond to data depicted in (a) and yellow crosses show the characteristic examples shown in figure 2(a). Three different regimes are highlighted following experimental data: I, oscillation; II, breakup; III, sheet formation. The grey solid line shows the correlation between We and W obtained from the two previous fits in (a,b), as illustrated by (3.2).

as the corresponding We increases with increasing laser-pulse energy. An empirical fit to the experimental data (θ_{open}, We) yields $\theta_{open} \sim We^{0.1}$, as illustrated in figure 3(a). The empirical scaling should be restricted to the relevant, validated range of We values, thus limiting the possible values of the opening angle. Experimental observations confirm that the opening angle θ_{open} approaches a limiting value of 90° at higher We . An immediate question arises as to whether this bulge corresponds to an impact-induced surface capillary wave (CW) travelling along the droplet. Considering the ‘deep pool’ limit (Lamb 1905, also see Denner, Paré & Zaleski 2017 or Ersoy & Eslamian 2019), the phase velocity of such a wave can be defined as

$$c \approx \left(\frac{2\pi\sigma}{\rho\lambda} \right)^{1/2}, \quad (3.1)$$

where λ is the wavelength and ρ the density of the tin droplet. The side view of the wave suggests a wavelength of $\lambda \sim 4 \mu\text{m}$, with phase velocity $c \sim 10 \text{ m s}^{-1}$. After 200 ns the displacement of such a wave would be around $2 \mu\text{m}$ which is negligible compared with the arc length observed between the upper and lower bulges (in the case of $\theta_{open} \sim 46^\circ$, this would be $\sim 100 \mu\text{m}$). This suggests that the observed early-time deformation is a result of the plasma pressure recoil on the droplet and relates θ_{open} with W . This relation is straightforwardly obtained from our simulations, as illustrated in figure 3(b), and a linear

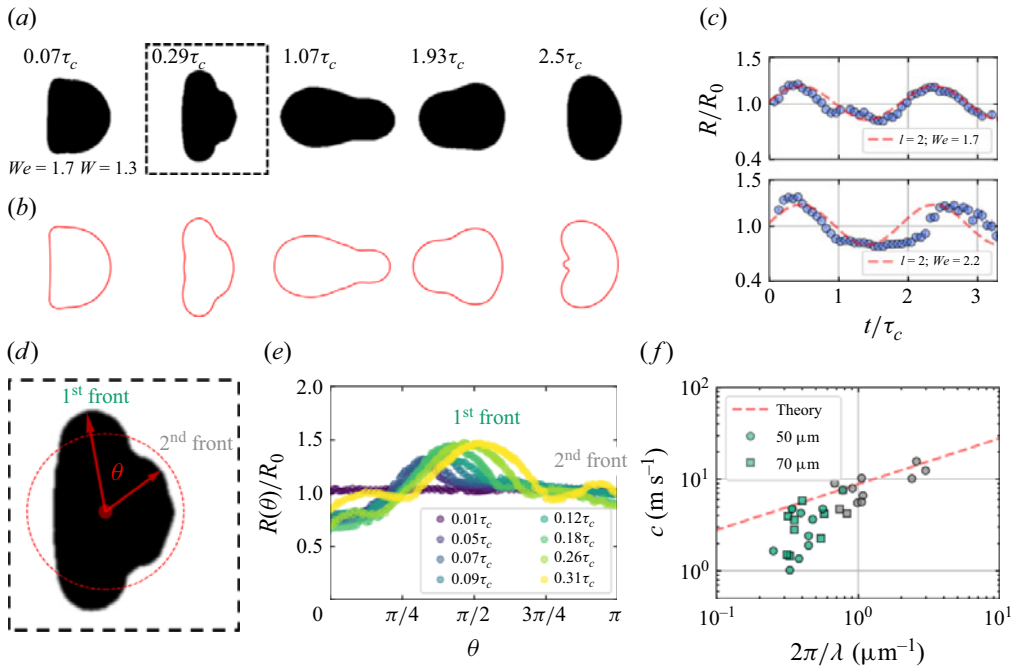


Figure 4. Droplet oscillation. (a) Shadowgraphs of droplet deformation within the oscillation regime at different fractions of capillary time τ_c for $We = 1.7$ and $W = 1.3$. (b) Numerical results at the same times as depicted in (a) and the same values for We and W . (c) Non-dimensional radius R/R_0 over time t/τ_c for two different oscillation cases: $We = 1.7$ and $W = 1.3$ (upper plot); $We = 2.2$ and $W = 1.4$ (lower plot). The red dashed line corresponds to the best fit of the oscillation estimated from the equation of Rayleigh modes with $l = 2$. (d) Example of a staircase-like structure where surface CWs are pointed out with red arrows as ‘1st front’ and ‘2nd front’. The red dashed circle represents the shape of the droplet at rest. Here, θ is the radial position of the CW front on the surface. (e) Parametric representation of the surface contour for different times t/τ_c as non-dimensional radial extension $R(\theta)/R_0$ against θ . The two CW fronts can be observed as two peaks. Data include droplet at rest (straight line at $0.01\tau_c$) and at several instances after impact to illustrate the origin and propagation of CWs. (f) The CW phase estimated for first (green data) and second (blue data) fronts. The red line represents the dispersion law described by (3.1).

fit to this simulation data yields $\theta_{open} \sim 48W + 3$. Using this relation, we obtain a good agreement between experiments and simulations, shown in figure 2. A closer inspection of the snapshots in figure 2(b) permits visualisation of the surface radial velocity, depicted by grey arrows. Note that the colourmap within the droplet also represents this radial velocity component. As argued by Gelderblom *et al.* (2016) and França *et al.* (2025), the radial velocity $u_{F_{def}}$ is a function of both the pressure profile and the maximum energy deposited and its maximum closely follows θ_{open} . Equating the observed scalings from figure 3(a,b), for the current experiment we can effectively correlate We with W and obtain the following empirical scaling relation:

$$W = \frac{(60We^{0.1} - 3)}{48}. \quad (3.2)$$

From (3.2), we can obtain the required input on W in the following. Besides the agreement between simulations and experiments at early times (see figure 2), these two parameters are sufficient to reproduce the droplet dynamics on the capillary time scale ($\sim 50 \mu\text{s}$), as shown in figure 4(a,b). The curve depicted in figure 3(c) represents the angular extension of the pressure profile on the droplet’s surface (W) and its variation

with We . Although we use an empirical fit to correlate We with W , let us consider a simple theoretical model. First, note that the separate relation between propulsion (We) and laser-pulse energy is well established (Kurilovich *et al.* 2016; Liu *et al.* 2020). The energy deposited on the droplet E_{od} is related to the pulse energy E_p as $E_{od} = E_p(1 - 2^{-D_0^2/d^2})$, where $d = 2\sigma_b$ is the diameter of the beam, with $\sigma_b = \text{FWHM}/2\sqrt{2\ln 2}$ with again the FWHM value $\approx 85 \mu\text{m} > D_0$. Second, the resulting propulsion velocity U of the droplet due to plasma recoil pressure scales with E_{od} as $U = k(E_{od} - E_{od,0})^{0.6}$, where $E_{od,0} \sim 0.04 \text{ mJ}$ is the offset related to a threshold of plasma formation and $k = 34 \text{ m s}^{-1} \text{ mJ}^{-0.6}$ is a numerical constant following Kurilovich *et al.* (2018) for a $D_0 = 47 \mu\text{m}$ case that is close to the current conditions. From this scaling, the dependence between E_{od} and propulsion-based We is obtained as

$$E_{od} = \left(\frac{We \sigma}{k^2 \rho D_0} \right)^{5/6} + E_{od,0}. \tag{3.3}$$

We next argue that the threshold for plasma formation together with the local laser intensity determines θ_{open} . The plasma threshold can be expressed in terms of laser intensity as the ratio between the threshold laser fluence F_{th} and pulse length: $I_{th} = F_{th}/\tau_p$, where $F_{th} = A^{-1} \rho \Delta H \sqrt{\mathcal{K} \tau_p}$ (see e.g. Chichkov *et al.* 1996 or Aden *et al.* 1992) with laser absorption coefficient A (see below), latent heat of evaporation $\Delta H = 2.5 \times 10^6 \text{ J kg}^{-1}$ and thermal diffusivity $\mathcal{K} = 16.4 \text{ m}^2 \text{ s}^{-1}$. The fluence of the laser beam is given by the ratio between the pulse energy and the beam area $F_p = E_p/\pi\sigma_b^2$. The resulting beam intensity projected on the droplet’s surface (see Reijers *et al.* 2018) can be defined as a function of θ (also see figure 1a):

$$I(\theta) = \cos \theta \exp \left[-\frac{\sin^2 \theta}{2\alpha^2} \right], \tag{3.4}$$

where $\alpha = \sigma_b/R_{eff}$ is the dimensionless ratio between the beam width and droplet’s effective radius. Here, $R_{eff} > R_0$, as a consequence of the plasma cloud formed on the laser-facing droplet pole, that effectively absorbs laser energy several micrometres away from the liquid surface. In our experimental range of low laser energies, close to the offset value $E_{od,0}$, where the plasma has not yet fully developed, it is, however, reasonable to consider a negligible plasma cloud radius and set $R_{eff} \approx R_0$. Note that in the case of $\text{FWHM} \gg D_0$, (3.4) reduces to to a much simpler form, $I(\theta) \sim \cos \theta$, enabling an analytical solution (see Appendix B). Combining (3.3) with (3.4), we obtain the total intensity projected on the droplet as

$$I_{od}(\theta) = \frac{1}{\tau_p \pi \sigma_b^2} \frac{1}{(1 - 2^{-D_0^2/d^2})} \left[\left(\frac{We \sigma}{k^2 \rho D_0} \right)^{5/6} + E_{od,0} \right] \cos \theta \exp \left[-\frac{\sin^2 \theta}{2\alpha^2} \right]. \tag{3.5}$$

This equation correlates We and θ with the laser intensity deposited on the droplet. If we consider that the plasma forms when the intensity on the droplet overcomes the intensity threshold, $I_{od}(\theta) > I_{th}$, we may estimate the radial position of plasma onset for a given We by equating $I_{od}(\theta_{open}) = I_{th}$ to yield an estimate for θ_{open} . The resulting model predictions (for $D_0 = 50 \mu\text{m}$) are displayed in figure 3(a) (also see Appendix B for further details). We note that this simple model reproduces the experimental data overall reasonably well for the given set of the corresponding parameters and leaving A as the sole free fit parameter to yield $A = 0.35$. We note that this best-fit value for A is higher than that previously reported by Meijer *et al.* (2022a) who used $A = 0.16$ derived from the Fresnel equations assuming no plasma formation, which may be due to the fact that inverse bremsstrahlung

absorption in the plasma increases laser absorption after plasma inception at the pole. The model excellently captures the experiment at higher We number, while overestimating the opening angle at the lowest We values. This behaviour at the lowest We may be expected given that (3.3) considers only integral energy values, not a local fluence, and the opening angle at low We is sensitive to $E_{od,0}$ (see Appendix B for further details). Furthermore, Kurilovich *et al.* (2018) also pointed out the difficulty in explaining the onset behaviour in (3.3) at low We even when employing full radiation hydrodynamics modelling. All in all, our simple model captures the essence of the behaviour: W increases monotonically with increasing We . In the following, we mainly focus on the influence of We and W on droplet deformation without further consideration of the underlying driving plasma dynamics. To this end, we use the empirical fit (3.2) that is fundamental for understanding the complete picture of droplet deformation driven by low-energy laser pulses. Furthermore, from (3.2) we learn that these two parameters are inherently correlated, as an increase in We implies a wider region of overlap for the plasma-induced pressure on the droplet. Finally, based on a qualitative inspection of our experimental data shown in figure 3(c), we classify the observed dynamical regimes of the droplet, namely capillary-driven oscillations, inertia-induced breakup and sheet formation (figure 1c–e), highlighted by the colourmap. In the following sections, we explain these behaviours in detail.

3.2. Droplet oscillation and surface waves

Starting from low-energy pulses, we first observe the droplet oscillation as described in § 1 and depicted in figure 4(a) where we show an example of oscillation at $We = 1.7$ and associated $W = 1.3$ (equation (3.2)). In figure 4(b), we display the numerical results at the same instants with the same values of We and W as in figure 4(a). Note the good agreement between the experimental data and the simulation. In figure 4(a,b), after the characteristic initial deformation, explained in the previous section, the droplet expands radially (see frames at $0.29\tau_c$). Here, the radial expansion rate is much lower than the propulsion velocity, i.e. $\dot{R}_0 \ll U$; therefore, capillary retraction overcomes any inertia-driven upward flow. Consequently, the droplet retracts and oscillates. If we trace the radial extension over time, as shown in the upper plot of figure 4(c), plotting the non-dimensionalised vertical half size, $R(\theta = \pi/2)/R_0$, over time, we clearly distinguish the first cycle of oscillation. Despite the complexity of shapes observed over time in figure 4(a), the overall temporal dynamics is surprisingly well described by a small-amplitude capillary-driven body oscillation, the so-called Rayleigh mode, with oscillation frequency $\omega_R^2 = \sigma l(l-1)(l+2)/(\rho R_0^3)$, where $l = 2$ as the fundamental mode for axisymmetric expansion/contraction. Rayleigh modes have also been studied in the context of free-flying droplets (Khismatullin & Nadim 2001; Bostwick & Steen 2009), pendant droplets (Basaran & DePaoli 1994; Moon, Kang & Kim 2006) and droplets flowing in different liquid media (Abi Chebel *et al.* 2012). In this particular case, for a droplet with $D_0 = 50 \mu\text{m}$, the oscillation period $t_R = 2\pi/\omega_R \approx 27 \mu\text{s}$. The assumption of small-amplitude oscillation appears reasonable given the maximum height within the first cycle, $\approx 0.2D_0 = 12 \mu\text{m} < D_0 = 50 \mu\text{m}$. Increasing We will make more liquid flow in the radial direction, resulting in stronger retraction and higher amplitude of oscillation. Indeed, we can see such an increase in amplitude in the bottom plot of figure 4(c) for $We = 2.0$. Moreover, in the bottom plot of figure 4(c) we notice that the overall oscillation dynamics is no longer described by the Rayleigh mode with $l = 2$. Instead, the curve quickly deviates from the theory, showing a long valley between $t \sim 0.5 \tau_c$ and $2.5 \tau_c$. This valley corresponds to a longer horizontal expansion of the droplet.

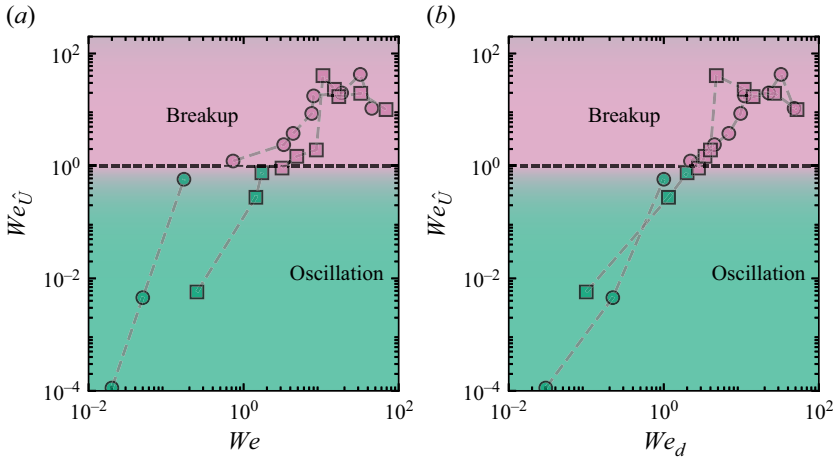


Figure 5. Droplet breakup. (a) Variation of the critical Weber number $We_{\hat{U}}$ based on the horizontal expansion rate \hat{U} after radial retraction over different propulsion Weber numbers We , for two different droplet diameters, $D_0 = 50, 70 \mu\text{m}$ (circle and square symbols, respectively). (b) Data from (a) with the horizontal axis represented by deformation Weber number We_d . The limit between oscillation and breakup regimes is estimated at $We_{\hat{U}} = 1$, as shown with the dashed line, with droplet oscillation for $We_{\hat{U}} < 1$ and droplet breakup for $We_{\hat{U}} > 1$.

A closer inspection of the droplet during its initial deformation reveals a staircase-like structure, particularly evident in figure 4(a,d) at $t = 0.29\tau_c$. This structure consists of successive capillary wavefronts triggered by laser impact, shaping the droplet as waves propagate. Similar patterns have been observed in droplet impact on solids (Renardy *et al.* 2003; Li, Wang & Dong 2019). Here, the laser pulse initiates CWs, driving liquid accumulation into a bulge that grows and propagates, forming subsequent wavefronts. Red arrows in figure 4(d) mark the various wavefronts. Interfacial contour profiles at different times, as shown in figure 4(e), illustrate the phase dynamics. The first CW front increases in amplitude and propagates azimuthally. Around $t = 0.31\tau_c$, a second front appears with a significantly lower amplitude. In some cases, for a larger droplet ($D_0 = 70 \mu\text{m}$), a third CW front is also observed. After estimating the wavelengths λ_{CW} from peak FWHM in figure 4(e), we plot phase velocity c versus wavenumber $k = 2\pi/\lambda_{CW}$ in figure 4(f), comparing experimental data for $D_0 = 50, 70 \mu\text{m}$ with (3.1). Green dots represent the first CW front, deviating from (3.1) as may be expected from its large amplitude ($R(\theta)/R_0 \sim 1.5$), invalidating the ‘deep pool’ assumption. In contrast, the second and third fronts, with lower amplitudes ($\lesssim 1.1R_0$), behave as surface CWs, closely following the predicted velocity. In conclusion, the oscillating droplet shows a complex combination of bulk oscillation and surface waves.

3.3. Droplet breakup

Droplets break up at large oscillation amplitudes. Hereafter, we refer to the horizontally stretched droplet as a filament, which expands horizontally at a certain velocity \hat{U} . Since the expansion of this filament is balanced by the kinetic energy of accumulating mass within the tip and the surface tension pulling back the filament, we can define the corresponding Weber number as $We_{\hat{U}} = \rho\hat{U}^2 D_f / \sigma$, where D_f is the characteristic diameter of the filament before the breakup. Figure 5(a) shows a monotonic increase of $We_{\hat{U}}$ with We , with the filament containing more mass that is moving at larger velocities,

with increasing We . This behaviour is well captured in figure 5(a) with the data points corresponding to two different droplet diameters following the same trend. Based on the balance between the inertia and capillary forces acting on the filament, we expect that the dominance of the tip inertia over capillary retraction will lead to the filament breakup. Conversely, if the surface tension overcomes the horizontal extension of the filament, the droplet will oscillate. A qualitative visualisation of the experimental data supports this argument, as we observe droplet oscillation for $We_{\hat{U}} < 1$ and droplet breakup for $We_{\hat{U}} > 1$ for both droplet sizes independently. This observation closely aligns with previous studies of inertia-driven breakup in liquid threads, insofar as they define a critical We for breakup (see Clanet & Lasheras 1999). Our critical Weber number $We_{\hat{U}}$ clearly captures the transition into breakup. However, the propulsion-velocity-based We alone does not dictate the breakup behaviour or determine $We_{\hat{U}}$. A highly focused pressure impulse (small W) may result in violent breakup even in the absence of significant propulsion. Indeed, we also observe different curves for different droplet diameters ($D_0 = 50, 70 \mu\text{m}$, circles and squares) when using We as the sole driving parameter. Instead, since the droplet oscillation/breakup is caused by the relative radial expansion and retraction, we invoke a more suitable parameter that is the deformation Weber number based on radial expansion rate, \dot{R}_0 , as $We_d = \rho \dot{R}_0^2 D_0 / \sigma$, ρ being the liquid tin density. Following Liu *et al.* (2022), we define \dot{R}_0 to be the velocity orthogonal to U : it captures the vertical expansion of the liquid. In figure 5(b) we rescale the horizontal axis with We_d and capture the variation of $We_{\hat{U}}$ that is now nearly invariant to the droplet diameter. Finally, we can observe that at much higher We_d values, the filament velocity gradually decreases. The slowing of the filament extension is due to the fact that, at higher We , even though the radial flow is stronger, the retraction becomes less effective as a sheet begins to develop.

3.4. Sheet formation

The dynamics of a radially expanding sheet following droplet impact at high We ($We \gtrsim 100$) has been well studied (see e.g. Villermaux & Bossa 2011; Wang *et al.* 2018) and we omit a detailed characterisation of this regime in the current work. Klein *et al.* (2020a) and Liu *et al.* (2022) demonstrated that, following a laser–droplet impact, the sheet expansion rate is accurately captured by the deformation Weber number, We_d , as defined in the preceding section. Indeed, the choice for We_d in § 3.3 was inspired by these works. The change in radius over time is described by balancing radial acceleration and surface tension continuously pulling back the sheet, resulting in the formation of a bounding thick rim (Wang *et al.* 2018), which is a source of ligaments and fragments that drain the sheet on the capillary time scale. Liu *et al.* (2022) illustrated that the time-varying radius of the sheet scales with We_d as $R(t)/R_0 \sim We_d^{1/2} f(t/\tau_c)$, for a considerably higher range of values for $We_d \sim 1000\text{--}10\,000$. The polynomial function $f(t/\tau_c)$ depends on the flow rate of the liquid from the sheet into the rim (see Wang & Bourouiba (2017) for details). This is due to the required radial acceleration that initiates the formation of the rim. According to Wang *et al.* (2018), this happens when local instantaneous capillary length equals the rim diameter, thus resulting in the local Bond number $Bo = \rho(-\ddot{R})b/\sigma = 1$, where \ddot{R} and b are sheet radial acceleration and rim thickness, respectively. This condition is fulfilled when the radial inertia overcomes the capillary retraction. In Appendix A, we present sample experimental data for sheet formation at $We_d \sim 300\text{--}1000$. For this study, we consider a sheet to be formed when the maximum radial extension of the liquid deformation exceeds twice the initial droplet radius, i.e. $R_{max} > 2R_0$. For the laser–droplet impact case, it is known that the maximum radius follows the relation $R_{max} - R_0 \sim 0.14\sqrt{We_d}R_0$ (see e.g. Liu *et al.* 2022; and see Villermaux & Bossa (2011)

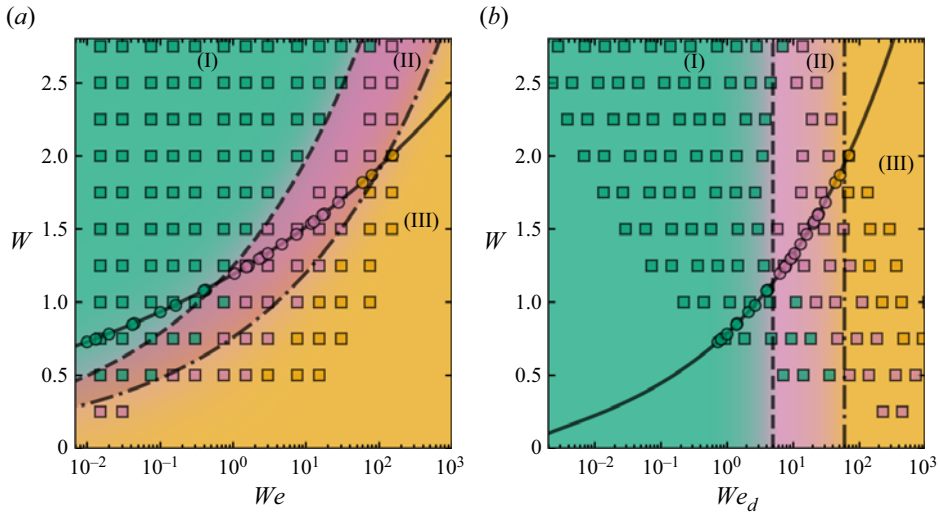


Figure 6. (a) Phase diagram of droplet dynamics as a function of centre mass propulsion We and pressure width W . Circles correspond to experimental data, while squares represent the simulations. Three different regimes are identified: oscillation (I), breakup (II) and sheet expansion (III). The black solid line corresponds to (3.2). Examples of each regime are illustrated in figure 1(c–e). (b) The same phase diagram but representing W as a function of We_d . Black dashed and dot-dashed lines in (a,b) represent the scaling $W \sim (We/We_d)^{1/5}$ with $We_d = 5$ and 60 as limits between oscillation/breakup and breakup/sheet formation regimes, respectively (see the main text). Note that these vertical lines are shown as curves in (a).

and Wang *et al.* (2018) for the droplet–pillar case) which indicates that the criterion for sheet expansion is met for $We_d = 60$. It is this criterion that establishes the second and last boundary in the phase map that is presented next.

3.5. Phase map

Using the criteria outlined above, the droplet behaviour analysed in previous sections can be portrayed in a single phase diagram based on the two key parameters: the pressure width W and impact We . As discussed in § 3.1, these two parameters are inherently correlated in the current experiments. However, via numerical computations we can build a two-dimensional map with We and W as independent parameters. In figure 6(a) we illustrate a combination of experimental data (circles) and simulations (squares) for a wide range of both parameters, and we define different regimes based on specific criteria. The corresponding scaling from (3.2) is depicted with a black line that necessarily goes through the experimental data points. We observe three well-defined regimes, corresponding to droplet oscillation (green area, (I)), droplet breakup (red area, (II)) and sheet formation (orange area, (III)). Recall that the transition between regimes (I) and (II) is straightforwardly identified in both experiments and simulations (breakup onset). To distinguish droplet breakup from sheet formation, we focus on the droplet maximum radial expansion. Recall that we choose the sheet formation onset as $R_{max} = 2R_0$. Considering previous studies in aerodynamic breakup of liquid droplets (see GuILDENBECHER *et al.* 2009), it is reasonable to invoke radial flow as an additional parameter to account for the underlying mechanism. Moreover, we have already discussed the relevance of radial expansion both for breakup onset (see § 3.3) and sheet formation. From our experiments (supported by simulations) we observe breakup onset at $We_d \sim 5$. Furthermore, the criterion $R_{max} = 2R_0$ is fulfilled at $We_d \sim 60$. Similar values were found in previous studies (see GuILDENBECHER *et al.* 2009; JACKIW & ASHGRIZ 2021) for droplet

breakup and sheet thinning behaviours. To obtain the explicit dependence of W with We and We_d , we recall our previous studies where these two non-dimensional numbers are related as $We_d \sim (\dot{R}_0/U)^2 We$ (see Hernandez-Rueda *et al.* 2022). Also, the term $(\dot{R}_0/U)^2$ strongly depends on the angular projection of the plasma generated upon laser impact. In the particular case of the raised cosine beam profile, we simulated the dependence of \dot{R}_0/U with W and determined an empirical scaling $\dot{R}_0/U \sim AW^{-5/2}$, with constant of proportionality $A \sim 3.8$ (also see the Appendix of França *et al.* 2025). If we insert this equation into the relation between two Weber numbers, we obtain $We_d \sim A^2 W^{-5} We$, which permits relating the pressure width W with propulsion We as $W \sim (We/We_d)^{1/5}$. This allows us to represent the phase diagram in terms of W and We_d as shown in figure 6(b). Effectively, we observe the limits as vertical lines, revealing that the transition between regimes is well captured by just the deformation Weber number, We_d . Note that, unlike Liu *et al.* (2022), who demonstrated the rescaling at high We ($\gg 100$), this phase diagram validates the principle at low We values (< 100), without the need for the presence of a thin sheet. Furthermore, our study identifies two additional morphologies that can be fully explained in terms of We_d . Separately, we note that the definition of We_d in the simulations, following França *et al.* (2025), slightly differs from that in the experiments: the simulations use the maximum velocity in the co-moving frame (which can be conveniently extracted already from the initialisation of the velocity field), which is not necessarily along the vertical r axis in the $r-z$ cylindrical coordinate frame (see figure 1). Any differences between the two definitions are minor, except for the cases with the smallest values of W (at large We) where the simulations overestimate We_d . Indeed, this difference in definition is partially responsible for the discrepancies in the phase diagram at low W values. The resulting phase diagram shows that oscillations occur for $We_d < 5$, the droplet breaks up for $5 \leq We_d \leq 60$ and a radially expanding sheet forms for $We_d > 60$, consistent with the condition $R_{max} = 2R_0$. Given these two values of We_d , the corresponding phase diagram can be represented in terms of W and We , where, based on the identified scaling, the vertical lines in figure 6(b) become curves in figure 6(a), following $W \sim We^{1/5}$.

4. Conclusions

In this work, we analyse the droplet dynamics upon nanosecond laser impact at low Weber numbers (0.1–100). Below the threshold of sheet formation, the droplet displays a complex interplay between radial flow and centre mass propulsion, leading to different deformation behaviours. We identify three regimes: droplet oscillation, breakup and sheet formation. After laser impact, the droplet radial expansion is followed by capillary-mediated retraction, resulting in axisymmetric oscillations. Droplet oscillations overall are found to follow the small-amplitude body motion characterised by Rayleigh modes. Superimposed on the body oscillations are CWs. We predominantly observe fundamental Rayleigh mode (expansion/retraction), with higher amplitudes as We is increased. Eventually, this leads to droplet breakup when the horizontal deformation is long enough. A critical Weber number $We_{\hat{c}}$ is introduced that captures the transition to breakup. We find that the whole dynamics is captured as a balance between the inertia of the horizontal motion and surface tension. Furthermore, we identify the role of the recoil pressure profile's radial distribution on the surface of the droplet and demonstrate that the higher the laser peak energy, resulting in higher We , the wider the pressure width, denoted by W . We show the intrinsic correlation between these two parameters that is present in the experiment. Complemented with simulations, we propose a phase diagram based on We and W , and study the droplet deformation as solely determined by pressure width,

propulsion velocity and radial deformation rate, captured by We_d as the single parameter defining the phase diagram.

Our studies closely correlate with industrial applications for nanolithography, where the source of EUV radiation is based on the interaction of nanosecond laser pulses with micro-sized liquid tin droplets. We extend the knowledge of previous studies on the topic towards the uncharted regime of low-energy laser pulses interacting with tin droplets. Furthermore, we highlight the role of surface radial distribution of the pressure profile and its correlation with the propulsion of the droplet. This relation is not evident from the case of the sheet formation, as it always comprises extreme We values which, given the aforementioned correlation, come with a large W .

Furthermore, the results of the present study not only deepen our understanding of low-amplitude droplet deformations, but also directly relate to other applications of laser–liquid interactions. For instance, in laser-induced forward transfer (Serra & Piqué 2019; Jalaal *et al.* 2019b; Das *et al.* 2024), where precise control of plasma formation near fluid and solid interfaces controls the jet formation (Jalaal *et al.* 2019a) or in laser ablation in liquids (Yang 2007; Yan & Chrisey 2012), where plasma ablates a solid target into the surrounding fluid. Nonetheless, many questions remain open. The detailed dynamics of laser-induced plasma at the liquid surface demands further investigations, since this ultrafast multiscale process crucially influences the fluid mechanism of the problem. More directly related to the present work, examining the complex mode composition within an oscillating droplet prior to breakup and understanding the transition from symmetric splitting to filament jetting are natural next steps.

Acknowledgements. This work was conducted at the Advanced Research Center for Nanolithography (ARCNL), a public–private partnership between the University of Amsterdam (UvA), Vrije Universiteit Amsterdam (VU), Rijksuniversiteit Groningen (UG), the Dutch Research Council (NWO), and the semiconductor equipment manufacturer ASML. Open access funding provided by Vrije Universiteit Amsterdam.

Funding. This work was partly financed by ‘Toeslag voor Topconsortia voor Kennis en Innovatie (TKI)’ from the Dutch Ministry of Economic Affairs and Climate Policy. The authors were supported by the European Research Council (ERC) under the European Union’s Horizon 2020 research and innovation programme (grant agreement no. 802648), and by the OTP grant (project number 19458) financed by the NWO. Open access funding provided by Vrije Universiteit Amsterdam.

Declaration of interests. The authors are not aware of any conflict of interest that might affect the objectivity of this study.

Data availability statement. The data that support the findings of this study are available from the corresponding author upon reasonable request.

Appendix A. Sheet formation

Upon high-energy laser impact, the droplet deforms radially with $\dot{R}_0 \sim U$ (see the main text). The expanding dynamics is determined by the formation of the bounding liquid rim. As shown in previous studies for laser–droplet interaction (see e.g. Klein *et al.* 2020a; Liu *et al.* 2022), radial extension is described by balancing the inertia of the rim and surface tension of the sheet. Following our studies of tin sheets, we describe the variation of the sheet radius through

$$\frac{2R}{D_0\sqrt{We_d}} = A (t/\tau_c)^3 + B (t/\tau_c)^2 + C (t/\tau_c) + D, \quad (\text{A1})$$

where the fitting parameters are $A = 0.33(5)$, $B = -0.92(5)$, $C = 0.57(2)$ and $D = 0.035(2)$. The numbers within parentheses are standard deviation uncertainty.

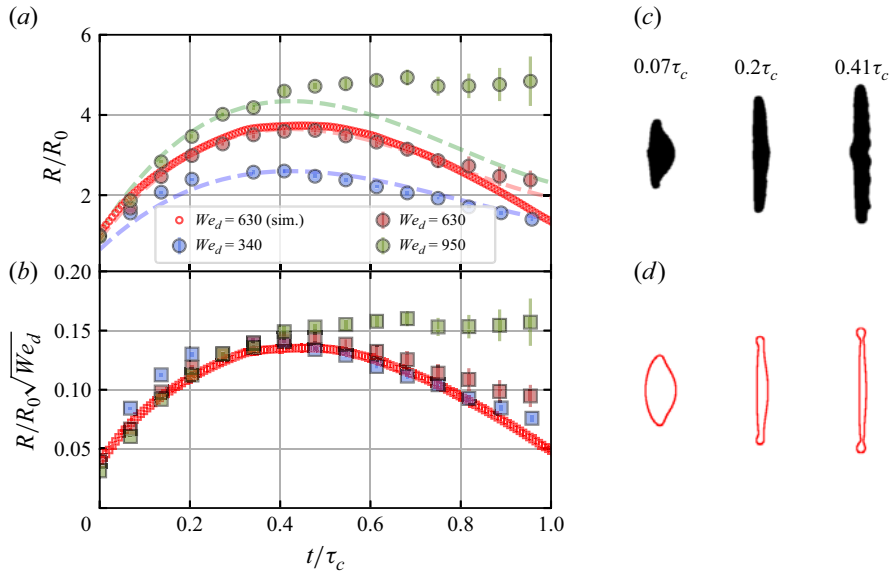


Figure 7. Radially expanding sheet formation. (a) Variation of the dimensionless sheet radius R/R_0 with time t/τ_c for four different We_d that includes experimental data: $We_d = 340, 670, 950$, and simulation: $We_d = 670$. The dashed lines represent (A1). (b) The collapse of the curves represented in (a) by rescaling the vertical axis with $R/R_0\sqrt{We_d}$. (c) Side-view frames of expanding thin sheet at three different instances depicted as fractions of capillary time for We_d and (d) frames obtained from simulations for $We_d = 670$.

In figure 7 we present expansion curves for $We_d = 340, 670, 950$. For comparison, we include simulated data for $We_d = 670$. We can see a qualitatively good match between (A1) and the experimental data in figure 7(a). In the particular case of $We_d = 950$, the sheet breaks before retraction, leading to a noticeable deviation from the theoretical curve at later times. In figure 7(b), we collapse the data from figure 7(a) onto a single curve by rescaling dimensionless radius with We_d , revealing the universal behaviour of the sheet. Finally, to illustrate the similarity between experimental observation and numerical simulations, in figure 7(c,d) we display frames at three different times.

Appendix B. Plasma onset and droplet deformation

Here we further detail the model developed in § 3.1. We assume that the opening angle θ_{open} observed in figure 2(a) corresponds to the largest angle θ where the plasma is still generated given a certain distribution of the projected intensity on droplet I_{od} together with a threshold intensity I_{th} . The intensity distribution is described by (3.5) for a given value of propulsion-based We . Equation (3.5) is solved numerically by equating $I_{od} = I_{th}$. We compute (3.5) for $FWHM = 85 \mu m$ and $D_0 = 50 \mu m$. The non-dimensional ratio between beam width and droplet effective radius is defined as $\alpha = \sigma/R_{eff}$. In the limit of small energy on droplet values (close to the offset value $E_{ed,0}$), we consider $R_{eff} \approx R_0$. We choose the absorption coefficient A as a (sole) free fit parameter given that beyond but near plasma threshold the laser absorptivity A will range between the value given by the Fresnel equations for an undisturbed liquid ($A \approx 0.15$ for unpolarised light) and that given by a fully developed plasma ($A \approx 1$). In figure 8(b) we show the result of a fit to the data leading to $A = 0.35$, a value indeed in the expected range. For the sake of comparison, in figure 8(a) we illustrate the intensity projection for different values of α . Note that the projection can be approximated by a cosine function for $\alpha \gg 1$ in which case it is possible

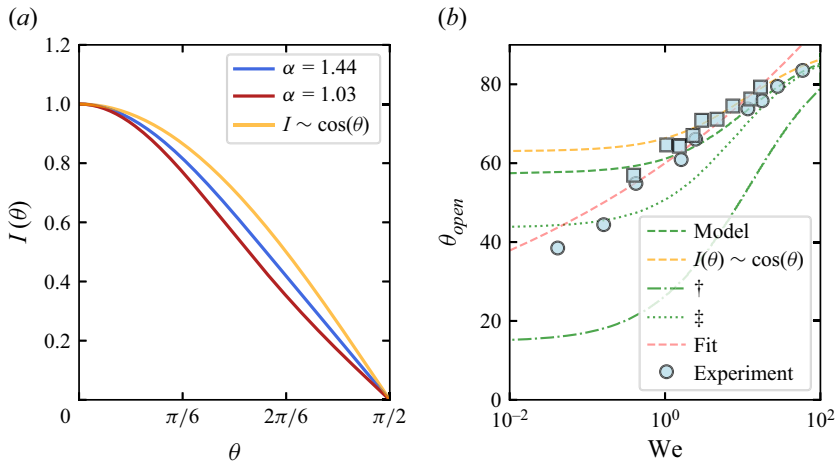


Figure 8. (a) Projection of laser intensity on a spherical surface. The intensity $I(\theta)$ variation against θ on the laser-facing droplet pole ($0-\pi/2$), for different laser width to droplet radius ratios: $\alpha = 1.44$ for $R_0 = 25 \mu\text{m}$ and $\alpha = 1.03$ for $R_0 = 35 \mu\text{m}$. The orange line represents the intensity projection as approximated by a cosine function $I(\theta) \sim \cos(\theta)$. (b) Variation of the opening angle θ_{open} with We . Blue circles ($R_0 = 25 \mu\text{m}$) and squares ($R_0 = 35 \mu\text{m}$) depict experimental observations as shown in figure 3(a). The green dashed line is the result of the numerical computation of (3.5). The red dashed line represents the empirical fit depicted by (3.2). The orange dashed line represents the analytical solution for θ in (3.5), when approximated by a cosine function ($\alpha \gg 1$ case). Additionally, we show two more solutions for (3.5): with values $A = 0.15$ and $E_{od,0} = 0.04 \text{ mJ}$ (\dagger) and with values $A = 0.35$ and $E_{od,0} = 0.025 \text{ mJ}$ (see appendix text for discussion).

to obtain an analytical solution to (3.5), resulting in $\theta \sim \arccos(We^{6/5})$. This solution is shown in figure 8(b) as an orange dashed line (taking $A = 0.35$ for this also). Since the range of laser fluences used for low- We dynamics is close to the threshold for plasma onset, it is not possible to elucidate the exact dynamics of plasma formation. We note that neither the numerical solution nor the cosine approximation fully accounts for the experimental observations in the range of We values. Notably, the higher deviations are observed at low values of $We < 0.1$. As explained in the main text, this regime might be characterised by a not fully developed plasma, giving rise to a highly non-trivial interplay between pressure profile and the projected laser intensity. Additionally, to clarify the influence of the choice of $E_{od,0}$, we next compute (3.5) for the same absorption coefficient $A = 0.35$ but using the offset value $E_{od,0}$ as the free parameter to match the lower regime. The resulting curve is depicted in figure 8(b) (\ddagger) with $E_{od,0} = 0.025 \text{ mJ}$. Note that this solution implies a lower plasma threshold than previously considered to describe the overall effect of plasma pressure leading to propulsion. It may well be that the threshold value found previously for the propulsion threshold (see e.g. Kurilovich *et al.* 2018), a result of integrated overall plasma pressure, does not represent well the local plasma dynamics. Indeed, the curve resulting from (3.5) for these input values (see figure 8b, \dagger) undershoots the experimental data. Furthermore, as noted by Kurilovich *et al.* (2018) no simple relation exists that accurately translates laser intensity to local plasma pressure.

REFERENCES

ABI CHEBEL, N., VEJRAŽKA, J., MASBERNAT, O. & RISSO, F. 2012 Shape oscillations of an oil drop rising in water: effect of surface contamination. *J. Fluid Mech.* **702**, 533–542.
 ADEN, M., BEYER, E., HERZIGER, G. & KUNZE, H. 1992 Laser-induced vaporization of a metal surface. *J. Phys. D: Appl. Phys.* **25** (1), 57.

- BASARAN, O.A. & DEPAOLI, D.W. 1994 Nonlinear oscillations of pendant drops. *Phys. Fluids* **6** (9), 2923–2943.
- BECKER, E., HILLER, W.J. & KOWALEWSKI, T.A. 1991 Experimental and theoretical investigation of large-amplitude oscillations of liquid droplets. *J. Fluid Mech.* **231**, 189–210.
- BOSTWICK, J.B. & STEEN, P.H. 2009 Capillary oscillations of a constrained liquid drop. *Phys. Fluids* **21** (3), 032108.
- CHICHKOV, B.N., MOMMA, C., NOLTE, S., VON ALVENSLEBEN, F. & TÜNNERMANN, A. 1996 Femtosecond, picosecond and nanosecond laser ablation of solids. *Appl. Phys. A* **63** (2), 109–115.
- CLANET, C. & LASHERAS, J.C. 1999 Transition from dripping to jetting. *J. Fluid Mech.* **383**, 307–326.
- DAS, A., GHOSH, A., CHATTOPADHYAYA, S. & DING, C.-F. 2024 A review on critical challenges in additive manufacturing via laser-induced forward transfer. *Opt. Laser Technol.* **168**, 109893.
- DENNER, F., PARÉ, G. & ZALESKI, S. 2017 Dispersion and viscous attenuation of capillary waves with finite amplitude. *Eur. Phys. J. Special Topics* **226** (6), 1229–1238.
- ERSOY, N.E. & ESLAMIAN, M. 2019 Capillary surface wave formation and mixing of miscible liquids during droplet impact onto a liquid film. *Phys. Fluids* **31** (1), 012107.
- FRANÇA, H., SCHUBERT, H.K., VERSOLATO, O.O. & JALAAL, M. 2025 Laser-induced droplet deformation: curvature inversion explained from instantaneous pressure impulse. arXiv preprint [arXiv: 2502.06417](https://arxiv.org/abs/2502.06417).
- GAI, G., HUET, D.P., GONG, J. & WACHS, A. 2025 Deformation, dynamics and rheology of immersed elastic capsules in an inertial shear flow. *J. Fluid Mech.* **1010**, A52.
- GELDERBLOM, H., LHUISSIER, H., KLEIN, A.L., BOUWHUIS, W., LOHSE, D., VILLERMAUX, E. & SNOEIJER, J.H. 2016 Drop deformation by laser-pulse impact. *J. Fluid Mech.* **794**, 676–699.
- GUAN, J.H., TAMIM, S.I., MAGOON, C.W., STONE, H.A. & SÁENZ, P.J. 2025 The way bubbles gallop. *Phys. Rev. Fluids* **10** (11), 110507.
- GULDENBECHER, D.R., LÓPEZ-RIVERA, C. & SOJKA, P.E. 2009 Secondary atomization. *Exp. Fluids* **46** (3), 371–402.
- HARRIS, D.M., ALVENTOSA, L., SAND, O., SILVER, E., MOHAMMADI, A., SYKES, T.C., CASTREJÓN-PITA, A.A. & CIMPEANU, R. 2026 Bouncing to coalescence transition for droplet impact onto moving liquid pools. *J. Fluid Mech.* **1030**, A16.
- HERNANDEZ-RUEDA, J., LIU, B., HEMMINGA, D.J., MOSTAFA, Y., MEIJER, R.A., KURILOVICH, D., BASKO, M., GELDERBLOM, H., SHEIL, J. & VERSOLATO, O.O. 2022 Early-time hydrodynamic response of a tin droplet driven by laser-produced plasma. *Phys. Rev. Res.* **4** (1), 013142.
- HIRT, C.W. & NICHOLS, B.D. 1981 Volume of fluid (VOF) method for the dynamics of free boundaries. *J. Comput. Phys.* **39** (1), 201–225.
- HSIANG, L.-P. & FAETH, G.M. 1992 Near-limit drop deformation and secondary breakup. *Intl J. Multiphase Flow* **18** (5), 635–652.
- JACKIW, I.M. & ASHGRIZ, N. 2021 On aerodynamic droplet breakup. *J. Fluid Mech.* **913**, A33.
- JALAAL, M., LI, S., KLEIN, S.M., QIN, Y. & LOHSE, D. 2019a Destructive mechanisms in laser induced forward transfer. *Appl. Phys. Lett.* **114** (21), 213703.
- JALAAL, M. & MEHRAVARAN, K. 2012 Fragmentation of falling liquid droplets in bag breakup mode. *Intl J. Multiphase Flow* **47**, 115–132.
- JALAAL, M. & MEHRAVARAN, K. 2014 Transient growth of droplet instabilities in a stream. *Phys. Fluids* **26** (1), 012101.
- JALAAL, M., SCHAARSBERG, M.K., VISSER, C.-W. & LOHSE, D. 2019b Laser-induced forward transfer of viscoplastic fluids. *J. Fluid Mech.* **880**, 497–513.
- JOSSERAND, C. & THORODDSEN, S.T. 2016 Drop impact on a solid surface. *Annu. Rev. Fluid Mech.* **48** (1), 365–391.
- KHISMATULLIN, D.B. & NADIM, A. 2001 Shape oscillations of a viscoelastic drop. *Phys. Rev. E* **63** (6), 061508.
- KLEIN, A.L., KURILOVICH, D., LHUISSIER, H., VERSOLATO, O.O., LOHSE, D., VILLERMAUX, E. & GELDERBLOM, H. 2020a Drop fragmentation by laser-pulse impact. *J. Fluid Mech.* **893**, A7.
- KLEIN, A.L., KURILOVICH, D., LHUISSIER, H., VERSOLATO, O.O., LOHSE, D., VILLERMAUX, E. & GELDERBLOM, H. 2020b Drop fragmentation by laser-pulse impact. *J. Fluid Mech.* **893**, A7.
- KURILOVICH, D., BASKO, M.M., KIM, D.A., TORRETTI, F., SCHUPP, R., VISSCHERS, J.C., SCHEERS, J., HOEKSTRA, R., UBACHS, W. & VERSOLATO, O.O. 2018 Power-law scaling of plasma pressure on laser-ablated tin microdroplets. *Phys. Plasmas* **25** (1), 012709.
- KURILOVICH, D., KLEIN, A.L., TORRETTI, F., LASSISE, A., HOEKSTRA, R., UBACHS, W., GELDERBLOM, H. & VERSOLATO, O.O. 2016 Plasma propulsion of a metallic microdroplet and its deformation upon laser impact. *Phys. Rev. Appl.* **6**, 014018.
- LAMB, H. 1905 On deep-water waves. *Proc. Lond. Math. Soc.* **2** (1), 371–400.

- LI, P.F., WANG, S.F. & DONG, W.L. 2019 Capillary wave and initial spreading velocity at impact of drop onto a surface. *J. Appl. Fluid Mech.* **12** (4), 1265–1272.
- LIU, B., HERNANDEZ-RUEDA, J., GELDERBLOM, H. & VERSOLATO, O.O. 2022 Speed of fragments ejected by an expanding liquid tin sheet. *Phys. Rev. Fluids* **7** (8), 083601.
- LIU, B., KURILOVICH, D., GELDERBLOM, H. & VERSOLATO, O.O. 2020 Mass loss from a stretching semitransparent sheet of liquid tin. *Phys. Rev. Appl.* **13**, 024035.
- LIU, B., MEIJER, R.A., HERNANDEZ-RUEDA, J., KURILOVICH, D., MAZZOTTA, Z., WITTE, S. & VERSOLATO, O.O. 2021 Laser-induced vaporization of a stretching sheet of liquid tin. *J. Appl. Phys.* **129** (5), 053302.
- LIU, B., MEIJER, R.A., LI, W., HERNANDEZ-RUEDA, J., GELDERBLOM, H. & VERSOLATO, O.O. 2023 Mass partitioning in fragmenting tin sheets. *Phys. Rev. Appl.* **20**, 014048.
- MEIJER, R.A., KURILOVICH, D., LIU, B., MAZZOTTA, Z., HERNANDEZ-RUEDA, J., VERSOLATO, O.O. & WITTE, S. 2022a Nanosecond laser ablation threshold of liquid tin microdroplets. *Appl. Phys. A* **128** (7), 570.
- MEIJER, R.A., KURILOVICH, D., EIKEMA, K.S.E., VERSOLATO, O.O. & WITTE, S. 2022b The transition from short- to long-timescale pre-pulses: laser-pulse impact on tin microdroplets. *J. Appl. Phys.* **131** (10), 105905.
- MOON, J.H., KANG, B.H. & KIM, H.-Y. 2006 The lowest oscillation mode of a pendant drop. *Phys. Fluids* **18** (2), 021702.
- MOU, Z., ZHENG, Z., JIAN, Z., ANTONINI, C., JOSSEERAND, C. & THORAVALL, M.-J. 2026 Singular jets and entrapments from compound drop impact. *Phys. Rev. Fluids* **11** (1), 013602.
- PARIK, A., TRUSCOTT, T. & DUTTA, S. 2024 On the threshold of drop fragmentation under impulsive acceleration. [arXiv: 2211.12017](https://arxiv.org/abs/2211.12017).
- PASANDIDEH-FARD, M., QIAO, Y.M., CHANDRA, S. & MOSTAGHIMI, J. 1996 Capillary effects during droplet impact on a solid surface. *Phys. Fluids* **8** (3), 650–659.
- PATEL, K. & ZHU, X. 2026 Direct numerical simulations of non-coalescing floating bubbles: geometry and self-organisation. *J. Fluid Mech.* **1026**, A19.
- PILCH, M. & ERDMAN, C.A. 1987 Use of breakup time data and velocity history data to predict the maximum size of stable fragments for acceleration-induced breakup of a liquid drop. *Intl J. Multiphase Flow* **13** (6), 741–757.
- POPINET, S. 2003 Gerris: a tree-based adaptive solver for the incompressible Euler equations in complex geometries. *J. Comput. Phys.* **190** (2), 572–600.
- POPINET, S. 2009 An accurate adaptive solver for surface-tension-driven interfacial flows. *J. Comput. Phys.* **228** (16), 5838–5866.
- POPINET, S. & Collaborators 2013–2021 Basilisk C. Available at: <http://basilisk.fr/>. Accessed on 01 01, 2024.
- POPINET, S. 2015 A quadtree-adaptive multigrid solver for the Serre–Green–Naghdi equations. *J. Comput. Phys.* **302**, 336–358.
- REIJERS, S.A., KURILOVICH, D., TORRETTI, F., GELDERBLOM, H. & VERSOLATO, O.O. 2018 Laser-to-droplet alignment sensitivity relevant for laser-produced plasma sources of extreme ultraviolet light. *J. Appl. Phys.* **124** (1), 013102.
- RENARDY, Y., POPINET, S., DUCHEMIN, L., RENARDY, M., ZALESKI, S., JOSSEERAND, C., DRUMRIGHT-CLARKE, M.A., RICHARD, D., CLANET, C. & QUR, D. 2003 Pyramidal and toroidal water drops after impact on a solid surface. *J. Fluid Mech.* **484**, 69–83.
- RIMBERT, N., ESCOBAR, S.C., MEIGNEN, R., HADJ-ACHOUR, M. & GRADECK, M. 2020 Spheroidal droplet deformation, oscillation and breakup in uniform outer flow. *J. Fluid Mech.* **904**, A15.
- SANJAY, V., LOHSE, D. & JALAAL, M. 2021 Bursting bubble in a viscoplastic medium. *J. Fluid Mech.* **922**, A2.
- SERRA, P. & PIQUÉ, A. 2019 Laser-induced forward transfer: fundamentals and applications. *Adv. Mater. Technol.* **4** (1), 1800099.
- THEOFANOUS, T.G. 2011 Aerobreakup of Newtonian and viscoelastic liquids. *Annu. Rev. Fluid Mech.* **43** (1), 661–690.
- TRYGGVASON, G., SCARDOVELLI, R. & ZALESKI, S. 2011 *Direct Numerical Simulations of Gas–Liquid Multiphase Flows*. Cambridge University Press.
- VERSOLATO, O.O. 2019 Physics of laser-driven tin plasma sources of EUV radiation for nanolithography. *Plasma Sources Sci. Technol.* **28** (8), 083001.
- VILLERMAUX, E. & BOSSA, B. 2011 Drop fragmentation on impact. *J. Fluid Mech.* **668**, 412–435.
- WANG, Y. & BOUROUIBA, L. 2017 Drop impact on small surfaces: thickness and velocity profiles of the expanding sheet in the air. *J. Fluid Mech.* **814** (1), 510–534.

- WANG, Y. & BOUROUIBA, L. 2021 Growth and breakup of ligaments in unsteady fragmentation. *J. Fluid Mech.* **910**, A39.
- WANG, Y., DANDEKAR, R., BUSTOS, N., POULAIN, S. & BOUROUIBA, L. 2018 Universal rim thickness in unsteady sheet fragmentation. *Phys. Rev. Lett.* **120**, 204503.
- YAN, Z. & CHRISEY, D.B. 2012 Pulsed laser ablation in liquid for micro-/nanosstructure generation. *J. Photochemistry Photobiology C: Photochemistry Rev.* **13** (3), 204–223.
- YANG, G.W. 2007 Laser ablation in liquids: applications in the synthesis of nanocrystals. *Prog. Mater. Sci.* **52** (4), 648–698.
- YARIN, A.L. & WEISS, D.A. 1995 Impact of drops on solid surfaces: self-similar capillary waves, and splashing as a new type of kinematic discontinuity. *J. Fluid Mech.* **283**, 141–173.
- ZHANG, B., SANJAY, V., SHI, S., ZHAO, Y., LV, C., FENG, X.-Q. & LOHSE, D. 2022 Impact forces of water drops falling on superhydrophobic surfaces. *Phys. Rev. Lett.* **129** (10), 104501.